Research Article

Nano Research
2022, 15(7): 6256–6265

ISSN 1998-0124 CN 11-5974/O4
https://doi.org/10.1007/s12274-022-4220-y

The morphology of hydroxyapatite nanoparticles regulates clathrin-mediated endocytosis in melanoma cells and resultant anti-tumor efficiency

Hongfeng Wu[1], Yuchen Hua[1], Jinjie Wu[1], Qin Zeng[1,2] (✉), Xiao Yang[1], Xiangdong Zhu[1,3] (✉), and Xingdong Zhang[1]

[1] *National Engineering Research Center for Biomaterials, Sichuan University, Chengdu 610064, China*
[2] *NMPA Key Laboratory for Quality Research and Control of Tissue Regenerative Biomaterials & Institute of Regulatory Science for Medical Devices & NMPA Research Base of Regulatory Science for Medical Devices, Sichuan University, Chengdu 610064, China*
[3] *Research Center for Materials Genome Engineering, Sichuan University, Chengdu 610064, China*

Received: 7 December 2021 / **Revised:** 6 February 2022 / **Accepted:** 7 February 2022

ABSTRACT

Clathrin-mediated endocytosis plays a critical role for hydroxyapatite nanoparticles (HANPs) to enter tumor cells, induce mitochondrial apoptosis, and inhibit tumor growth. This study was aimed to investigate how the morphology of HANPs impacts the endocytosis of the particles in melanoma cells, and their anti-tumor effect by using *in vitro* cell experiments and *in vivo* tumor animal model. Three shapes of HANPs, including granular HANPs (G-HANPs), rod-like HANPs (R-HANPs), and needle-like HANPs (N-HANPs), were successfully prepared by wet chemical method. All the three HANPs could be internalized into A375 melanoma cells as indicated by cellular transmission electron microscopy images. Among these HANPs, only G-HANPs induced morphological change of mitochondria and loss of mitochondrial membrane potential ($\Delta\psi_m$), and exhibited the greatest intracellular internalization efficiency in the tumor cells. Furthermore, the results of immunofluorescence staining and western blotting indicated that the level of adaptin-2 (AP2) protein was up-regulated by all the HANPs, and highest in G-HANPs treated A375 cells. Moreover, in the tumor-bearing mouse model, we found that tumor growth was delayed by all the three HANPs, of which, G-HANPs delayed tumor growth most efficiently and presented a highest expression level of AP2 protein in tumor tissues. Therefore, this study suggested that the morphology of HANPs regulated their endocytosis efficiency and their effect to inhibit tumor growth. This work facilitates to direct the rational design of nano-materials for tumor therapy.

KEYWORDS

hydroxyapatite nanoparticles, adaptin-2 protein, morphology, endocytosis, anti-tumor effect

1 Introduction

Hydroxyapatite (HA, $Ca_{10}(PO_4)_6(OH)_2$) is the main inorganic component of human bones and teeth, which has been widely used in the biomedical fields such as bone tissue repairs and drug delivery carriers due to its good biocompatibility and bioactivity [1–3]. Another emerging biomedical application for HA is tumor therapy since its anti-tumor activity was first reported *in vitro* in 1993 [4–8]. So far, the mechanism by which HA nanoparticles (HANPs) inhibit tumor growth has not been fully elucidated. Some studies demonstrated that HANPs can enter tumor cells through clathrin-mediated endocytosis (CME), activate mitochondria dependent apoptosis pathway, inhibit tumor cell proliferation, and eventually induce tumor cell apoptosis in a dose dependent manner [9, 10]. Previous studies have revealed that the anti-tumor performance of HANPs is positively correlated with CME, and the physiochemical features of HANPs also play an important role in CME [6, 11, 12]. Therefore, CME plays a critical role for HANPs to prevent tumor growth.

CME, marked by clathrin-coated vesicles (CCVs), is a classical pathway for the internalization of cell surface and extracellular molecules in eukaryotes [13–15]. Endocytosis of cargo passing through CME is mediated by its specific transmembrane receptors, mainly from the cell surface into CCVs [16, 17]. The formation of CCVs starts from the recruitment of coated proteins, including clathrin and adaptin-2 (AP2) protein, on the cytosolic side of the plasma membrane [16]. The heterotetrameric AP2 protein is a unique member of the clathrin adaptor complex family, which plays a central role in CME by means of recruiting cargo and clathrin to endocytosis sites [18–20]. AP2 protein is consisted of four subunits, including a small σ2 subunit (about 20 KD), a medium μ2 subunit (about 50 KD), and two large α2 and β2 subunits (about 100 KD). Each unit has its own function. σ2 subunit is responsible for the structural stability of AP2 protein, α2 and β2 subunits are responsible for forming clathrin cages by connecting with clathrin and other accessory proteins around the vesicle membrane, and μ2 subunit is mainly responsible for recognition and interaction with the receptor structures [18, 21, 22]. AP2 is also involved in a series of biological processes, including cell growth, cell signaling, and so on [19, 23].

In previous studies, we synthesized five HANPs with different material properties, and studied their anti-melanoma effects *in vitro* and *in vivo*. The results showed that five HANPs could

Address correspondence to Qin Zeng, qzeng8156@scu.edu.cn; Xiangdong Zhu, zhu_xd1973@scu.edu.cn

activate mitochondria-related apoptosis pathways and inhibit the proliferation of melanoma cells [7]. Zhu et al. used molecular dynamics models to investigate the binding of spherical HANPs, rod-like HANPs (R-HANPs), needle-like HANPs (N-HANPs), and AP2-μ2 protein at the atomic level. They found that the morphology of the NPs determined the binding affinities upon AP2-μ2 protein through electrostatic interaction, and spherical HANPs significantly changed the conformation toward AP2-μ2 protein [24]. However, this was not validated with cell experiments or animal studies.

Therefore, in the present study, three kinds of HANPs with different typical morphology (granular, rod-like, and needle-like) were synthesized to explore how the morphology of HANPs impacts their endocytosis into melanoma cells and anti-tumor effect *in vivo* (Fig. 1). Our result demonstrates that HANPs could manipulate the expression level of AP2, endocytosis of cargo, and anti-tumor effect through controlling their morphology.

2 Materials and methods

2.1 Materials

Fetal bovine serum (FBS) was purchased from Thermo Fisher Scientific, Gibco, USA. Dulbecco's modified Eagle medium (DMEM), 1% penicillin-streptomycin solution, phosphate buffered solution (PBS), trypsin-0.25%, and ethylene diamine tetraacetic acid (EDTA) were purchased from Hyclone, USA. JC-1 MitoMP Detection Kit was purchased from Dojindo Laboratories, Japan. Fluorescein isothiocyanate (FITC), tetramethylrhodamine (TRITC)-Phalloidin, and goat serum were purchased from Beijing Solarbio Science & Technology Co. Ltd., China. Matrigel was purchased from BD Biosciences, USA. Chlorpromazine hydrochloride was purchased from MedChemExpress LLC, USA. Tris-HCl solution was purchased from Chengdu Kelong Chemical Reagent Co. Ltd., China. Cy5-labeled goat anti-rabbit and Cy3-labeled donkey anti-goat secondary antibodies were obtained from Servicebio, China. 2-(4-Amidinophenyl)-6-indolecarbamidine dihydrochloride (DAPI) and Fluo-3 AM were purchased from Beyotime Institute of Biotechnology, China. Goat-anti-human AP2-α2 protein, rabbit-anti-human AP2-μ2 protein, Ki-67 primary antibody, and CD31 primary antibody were purchased from Abcam, UK. The TUNEL kit was purchased from Roche, Switzerland.

2.2 Cell and animals

The human A375 melanoma cell line was purchased from iCell Bioscience Inc, China. The A375 cells were cultured in DMEM containing 10% FBS and 1% penicillin-streptomycin solution at 37 °C in an atmosphere of 5% CO_2 and 95% humidity.

Five-week-old female Balb/c nude mice (weighing 16.23 ± 0.80 g) purchased from GemPharmatech Co. Ltd. (China) were used for establishing the A375 melanoma model *in vivo*. All animal proposals were approved by the Animal Care and Use Committee of Sichuan University according to the guidelines of the Chinese Society of Laboratory Animals on animal welfare.

2.3 Preparation and characterization of HANPs

The three HANPs with different morphologies, including granular HANPs (G-HANPs), R-HANPs, and N-HANPs, were synthesized using wet chemical method as described in our previous studies [7]. The phase composition of HANPs was identified by X-ray diffracion (XRD, Shimazu XRD-6100, Japan). The morphology, size, and the selected area electron diffraction (SAED) of HANPs were determined by transmission electron microscopy (TEM, Tecnai G2F20, FEI, USA). Based on the TEM images, the size of HANPs was measured by Nano Measure software.

2.4 Release of Ca^{2+}

According to the protocol previously described [7], the three HANPs were allowed to stay in Tris-HCl solution, pH = 7.4 or 5.5, at the concentration of 200 μg/mL for 1 or 3 days. The supernatant was collected, and the Ca^{2+} concentration in the supernatant was determined by the inductively coupled plasma-optical emission spectroscopy (ICP-OES, ARCOS, Spectro Analytical Instruments GmbH, Germany).

2.5 Cell ultrastructure morphology observation

In order to observe the internalization of HANPs in A375 cells and the ultrastructural change of HANPs treated cells, after the three HANPs suspensions were respectively co-cultured with A375 cells at the concentration of 200 μg/mL for 3 days in culture dishes, the cells were collected and sectioned according to the

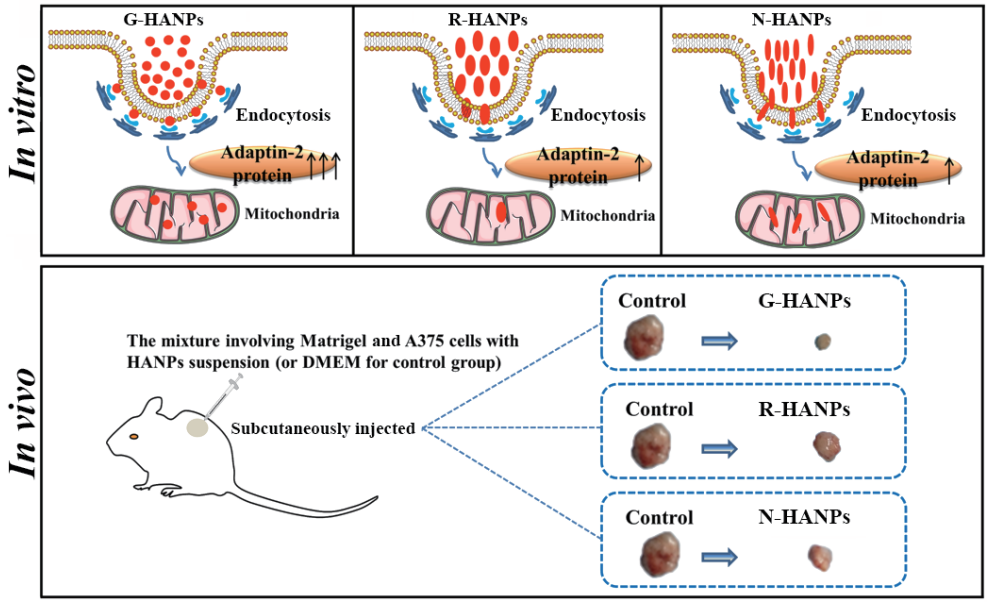

Figure 1 Schematic illustration of anti-tumor activity of HANPs controlled by their morphology. HANPs modulate the expression level of AP2 protein as a function of their morphology, which lead to difference in internalization efficiency of the particles, induction of abnormal mitochondrial production *in vitro*, and inhibition of tumor growth *in vivo*.

protocol in a previous study [25], and then examined using biological TEM (JEM-1400Plus, JEOL, Japan).

2.6 Evaluation of mitochondrial membrane potential ($\Delta\psi_m$)

$\Delta\psi_m$ of HANPs treated tumor cells was evaluated using JC-1 MitoMP Detection Kit. After the three HANPs suspensions were co-cultured with A375 cells at the concentration of 200 μg/mL for 1 or 3 days in a 24-well plate, the cells were washed with PBS, trypsinized, collected, and re-suspended in 2 μmol/L JC-1 working solution, and incubated for 30 min in the dark at 37 °C in an atmosphere of 5% CO_2. Next, the cells were washed twice with Hank's balanced salt solution (HBSS), soaked in imaging buffer solution, and analyzed by fluorescence microplate reader (Green, *Ex*/*Em* = 488/525 nm; Red, *Ex*/*Em* = 535/585 nm; Synergy H1, BioTek, USA).

2.7 Intracellular Ca^{2+} level

The level of the intracellular Ca^{2+} concentration was measured by the fluorescence probe for intracellular Ca^{2+}, Fluo-3 AM. A375 cells were seeded in a 24-well plate at a density of 1×10^4 cells/well for 24 h, and then treated with the three HANPs suspensions at the concentration of 200 μg/mL, respectively. After co-culture for 1 or 3 days, the culture media were removed, and the cells were washed with PBS, trypsinized, collected, and loaded with Fluo-3 AM dye (1 μM) at 37 °C for 40 min in the dark. After being washed twice to remove the free Fluo-3 AM dye, the cells were soaked in PBS at 37 °C for 20 min and immediately detected by a fluorescence microplate reader (Green, *Ex*/*Em* = 488/525 nm).

2.8 Cellular uptake assay

The intracellular uptake efficiency of HANPs was then determined by confocal laser scanning microscopy (CLSM, Zeiss LSM880, USA) and flow cytometry (FCM, BD FACSCanto II). The three HANPs were labeled with FITC (Solarbio, China) according to a reported method [26]. Before being treated to cells, the three FITC labeled HANPs were repeatedly washed with PBS (pH = 7.4, Hyclone, USA) until HANPs were colorless at the bottom of the centrifuge tube.

To observe the localization of HANPs by CLSM, A375 cells were seeded in 24-well glass bottomed plates at a density of 1×10^4 cells/wellfor24hpriortoco-culturewiththethreeFITC-HANPs(*Ex*/*Em* = 488/520 nm) at the concentration of 200 μg/mL. 1 or 3 days later, the cells were washed with PBS to remove free HANPs, fixed with 4% paraformaldehyde for 10 min, stained with TRITC-Phalloidin (Solarbio, China) (*Ex*/*Em* = 543/580 nm) for 30 min, and followed by DAPI (Beyotime, China) (*Ex*/*Em* = 405/454 nm) staining for 5 min at room temperature (RT). The stained cells were examined by CLSM.

FCM was used to quantify the intracellular uptake of HANPs, 3×10^4 A375 cells/well were seeded in a 12-well plate for 24 h and treated with the three FITC-HANPs (*Ex*/*Em* = 488/520 nm) at the concentration of 200 μg/mL. After co-culture for 4 h, 1 or 3 days, the media were removed, and the cells were washed with PBS, trypsinized, collected, re-suspended in ice-cold fluorescence-activated cell sorting (FACS) buffer, and determined by FCM.

Additionally, to verify the role of CME in endocytosis of HANPs, A375 cells were seeded in a 12-well plate at a density of 3×10^4 cells/well for 24 h, followed by another 1 h incubation with the CME inhibitor, chlorpromazine hydrochloride (10 μg/mL), at 37 °C. Then the culture media were removed. The cells were washed, treated with the three FITC-HANPs at the concentration of 200 μg/mL for 1 day, and finally analyzed by FCM.

2.9 Immunofluorescence staining

Immunofluorescence staining experiment was used to investigate the interaction between HANPs and AP2-α2 or AP2-μ2 protein. The A375 cells (2×10^4 cells/well) in 24-well glass bottomed plates were treated with HANPs or FITC-HANPs at the concentration of 200 μg/mL for 1 or 3 days. The culture medium was discarded, and the cells were washed and fixed with 4% paraformaldehyde for 20 min, permeabilized with 0.5% Triton X-100 for 20 min, and blocked with 10% goat serum (Solarbio, China) at 37 °C for 30 min. Then the cells were incubated with the AP2-α2 protein (1:200, ab189995, Abcam, UK) or AP2-μ2 protein (1:350, ab218107, Abcam, UK) primary antibody overnight at 4 °C. Then the cells were incubated with cy3-labeled (*Ex*/*Em* = 550/570 nm) or cy5-labeled (*Ex*/*Em* = 648/662 nm) secondary antibody (Servicebio, China) for 1 h at 37 °C. After DAPI staining for 5 min at RT, the cells were examined by CLSM.

2.10 Western blotting analysis

The protein expression level of AP2-μ2 in A375 cells was analyzed by Western blotting after HANPs treatment. The cells were seeded in 6 well plates with a density of 2×10^4 cells/well. After overnight incubation, the cells were treated with HANPs (200 μg/mL) for 1 or 3 days. In the following, the cells were lysed using Trizol reagent (Beyotime, China) and centrifuged at 12,000 rpm/min for 15 min at 4 °C. The concentration of total protein in the cell lysate was determined by bicinchoninic acid (BCA) method (Beyotime, China). 15 μg protein in each group was loaded onto SDS-polyacrylamide gel (Biofroxx, Germany), separated by electrophoresis at 100 V for 2 h, and then transferred to polyvinylidene fluoride (PVDF) membrane (Sigma-Aldrich, USA). After being blocked with tris buffered saline with tween (TBST, 0.1% Tween-20, 10% tri-sec-buffer saline, and 89.9% deionized (DI) water) including 5% fat-free milk (Beyotime, China), the membranes were incubated with monoclonal primary antibody of AP2-μ2 protein (1:1000, ab218107, Abcam, UK) at 4 °C overnight and then with secondary antibody. The enhanced chemiluminescence (ECL) kit (Affinity, China) with a ChemiDocTM XRS+imaging system (Bio-Rad, USA) was then used to observe the immunoreactive blots.

2.11 Anti-tumor evaluation of HANPs *in vivo*

All nude mice were randomly divided into 4 groups (n = 6): control group (Control), G-HANPs treated group (G-HANPs), R-HANPs treated group (R-HANPs), and N-HANPs treated group (N-HANPs). The mixture of Matrigel (50 μL, 356234, BD, USA), A375 cells (1×10^6), and 50 μL HANPs suspension (50 mg/kg) or DMEM for control group, was subcutaneously injected into the back of the mice to observe the tumor growth [4, 7]. The mice were weighed every 2 days, and the length and width of tumor were measured by a vernier caliper and calculated according to the formula: Tumor volume (mm^3) = 0.5 × (length × $width^2$) [27, 28]. 35 days later, all mice were sacrificed, and the tumor tissues were excised, weighed, immediately fixed in 10% neutral formalin solution, embedded in paraffin, and sectioned into 4 μm thick slides for Hematoxylin-Eosin (H&E) staining. Immunocytochemistry staining was also performed to observe the expression of Ki-67 (1:100, ab16667, Abcam, UK), CD31 (1:400, ab28364, Abcam, UK), TUNEL (Roche, Switzerland), and AP2-μ2 protein (1:800, ab218107, Abcam, UK).

2.12 Biosafety evaluation of HANPs *in vivo*

When tumors were isolated in the above experiment, the main organ samples including heart, liver, spleen, lung, and kidney were isolated for H&E staining, and the whole blood was collected via

cardiac punctures for blood routine examination using an automatic hematology analyzer (BC-2800Vet, Mindray, Shenzhen, China). The serum sample was obtained by the centrifugation of the whole blood at 5,000 rpm/min for 15 min. The levels of alanine aminotransferase (ALT), aspartate aminotransferase (AST), creatinine (CREA), urea, blood calcium (Ca), and blood phosphorus (*P*) in the serum were determined using an automatic biochemical analyzer (BS-240VET, Mindray, Shenzhen, China).

2.13 Statistical analysis

All experimental data were presented as mean ± standard deviation (SD). Each experiment was carried out in triplicate. One-way analysis of variance (ANOVA) was carried out using SPSS 20.0 software for the statistical analyses. $P < 0.05$ and $P < 0.01$ were considered statistically significant.

3 Results

3.1 Characterization of the nanoparticles

In the present study, the three HANPs with different morphologies were prepared by wet chemical method. The phase composition, morphology, and size of the as-prepared HANPs were characterized by XRD and TEM, respectively. The XRD result showed that the characteristic peaks of the three HANPs were consistent with those of the HA standard (JCPDS: 09-0432), indicating that all the three HANPs were pure phase (Fig. 2(a)). TEM images identified that the three HANPs were nano-sized with three typical morphologies, granular, rod-like, and needle-like. The G-HANPs were 17.41 ± 1.16 nm in diameter. The R-HANPs showed an average size of 45.13 ± 8.85 nm in length and 25.24 ± 2.12 nm in width. The N-HANPs had an average length of 39.29 ± 6.05 nm and a width of 5.88 ± 0.74 nm (Fig. 2(b)). The SAED results indicated that all the three HANPs were polycrystallinity, which was indicated by multiple circles (Fig. 2(b)).

3.2 Biological TEM, $\Delta\psi_m$, and intracellular Ca^{2+} in the tumor cells

The biological TEM measurement was used to investigate whether HANPs could be internalized into cells and the morphological changes of cellular ultrastructure after A375 cells were treated with the three HANPs. The TEM images obviously showed that all the three HANPs were localized in the cells, indicating the intracellular uptake of HANPs by the tumor cells. Some representative abnormal characteristics including typical mitochondrial swelling were observed only in the cells treated with G-HANPs (Fig. 3(a)) [29]. We further observed only G-HANPs treated cells, but not R-HANPs or N-HANPs, exhibited the loss of

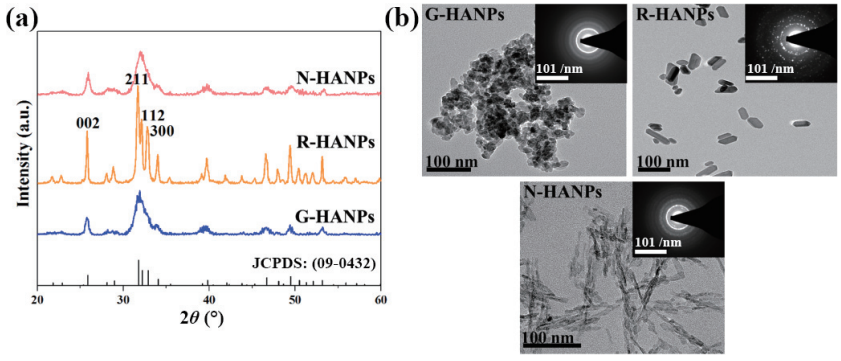

Figure 2 The three nano-sized HANPs with different shapes were synthesized and characterized. (a) XRD patterns of the three HANPs. (b) Representative TEM and SAED (insets at the top-right corners) images of the three HANPs.

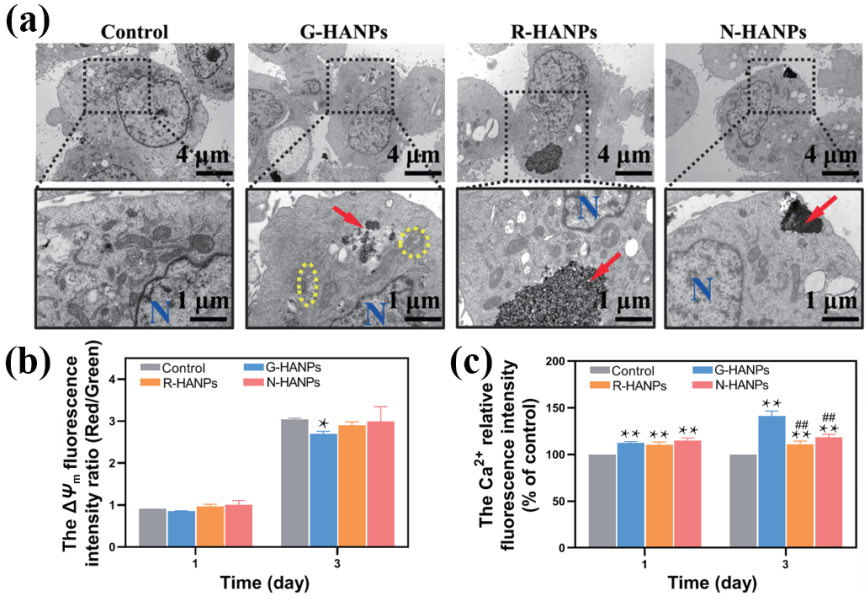

Figure 3 The G-HANPs induced the loss of $\Delta\psi_m$ and a highest level of intracellular Ca^{2+} in the tumor cells. (a) TEM images of A375 cells after the cells were treated with the three HANPs at the concentration of 200 μg/mL for 3 days (red arrow: HANPs, yellow dotted box: swollen mitochondria, and N: nucleus). (b) The $\Delta\psi_m$ fluorescence intensity ratio (Red/Green) of A375 cells after the cells were treated with the three HANPs at the concentration of 200 μg/mL for 1 or 3 days ($n = 3$; vs. Control, $^*P < 0.05$ and $^{**}P < 0.01$). (c) The relative Ca^{2+} fluorescence intensity of A375 cells after the cells were treated with the three HANPs at the concentration of 200 μg/mL for 1 or 3 days ($n = 3$; vs. Control, $^*P < 0.05$ and $^{**}P < 0.01$; vs. G-HANPs, $^{\#}P < 0.05$ and $^{\#\#}P < 0.01$).

$\Delta\psi_m$ after 3 days co-culture of particles and cells, suggesting the induction of mitochondrial apoptosis by G-HANPs (Fig. 3(b)). Moreover, G-HANPs stimulated the highest levels of intracellular Ca^{2+} in A375 cells (Fig. 3(c)).

3.3 Intracellular uptake assay

Furthermore, the cellular uptake of fluorescence labeled HANPs by A375 cells was analyzed qualitatively and quantitatively using CLSM and FCM. The results from CLSM confirmed the three HANPs were able to enter the A375 cells after 1- or 3-day incubation of particles and A375 cells. Moreover, no obvious morphology changes of the cytoskeleton and nucleus were observed in the control groups without particles. But 1 or 3 days incubation of cells and G-HANPs, or 1 day incubation of N-HANPs induced the appearance of cell plasma membrane bubbling, which is a typical sign for cell apoptosis (Figs. 4(a) and 4(b)) [30]. The quantitative analysis by FCM demonstrated a highest mean fluorescence intensity (MFI) of A375 cells treated with G-HANPs among those treated with the three HANPs (Figs. 4(c)–4(h)). Together, the results obtained indicated that among the three HANPs, G-HANPs showed the greatest endocytosis efficiency in the tumor cells. Additionally, the addition of CME inhibitor, chlorpromazine hydrochloride, significantly decreased the intracellular efficiency in A375 cells, indicating that CME pathway mediated the internalization of HANPs into A375 cells (Fig. S2 in the Electronic Supplementary Material (ESM)).

3.4 AP2 protein expression in HANPs treated tumor cells

We already know that the morphology of HANPs impact their endocytosis efficiency. Next, we studied the interaction between AP2 protein and HANPs *in vitro* by immunofluorescence staining and Western blotting assays. After one-day incubation of cells and the three HANPs, the CLSM images from immunofluorescence staining showed that AP2-α2 enriched in the cell plasma around nuclear, and the fluorescence intensity of AP2-α2 increased in the cells treated with the three HANPs, compared with the control group. Moreover, the cells treated with G-HANPs showed the highest fluorescence intensity of AP2-α2. These results suggested that HANPs could up-regulate the expression of AP2-α2 protein, and G-HANPs had the greatest effect on it (Figs. 5(a) and 5(b)). But this effect was not observed after 3-day incubation (Figs. 5(c) and 5(d)).

We also detected the expression of AP2-μ2 after 1 or 3 days incubation of cells and the three HANPs, and the CLSM images indicated that the fluorescence intensity of AP2-μ2 was stronger for HANPs treated cells than that for the control group. At day 1, fluorescence labeled NPs clustered around AP2-μ2 in the three HANPs. However, at day 3, the intensity of fluorescence labeled R-HANPs or N-HANPs obviously decreased (Figs. 6(a) and 6(b)).

We further quantified the expression level of AP2-μ2 protein from A375 cells in the presence of HANPs by Western blotting. The results showed that compared with the control group, the expression level of AP2-μ2 protein from A375 cells increased after HANPs treatment for 1 or 3 days. Among the three HANPs, G-HANPs led to a highest level of AP2-μ2 protein in A375 cells (Figs. 6(c)–6(f)). These results indicated that the expression level of AP2 protein in A375 cells could be regulated by the morphology of HANPs, and the G-HANPs exhibited the greatest effect.

3.5 Evaluation on the anti-tumor efficacy of the HANPs *in vivo*

We further evaluated the anti-tumor effect of the three HANPs in an A375 melanoma-bearing Balb/c nude mouse model. After subcutaneous inoculation of tumor cells and HANPs, the tumor

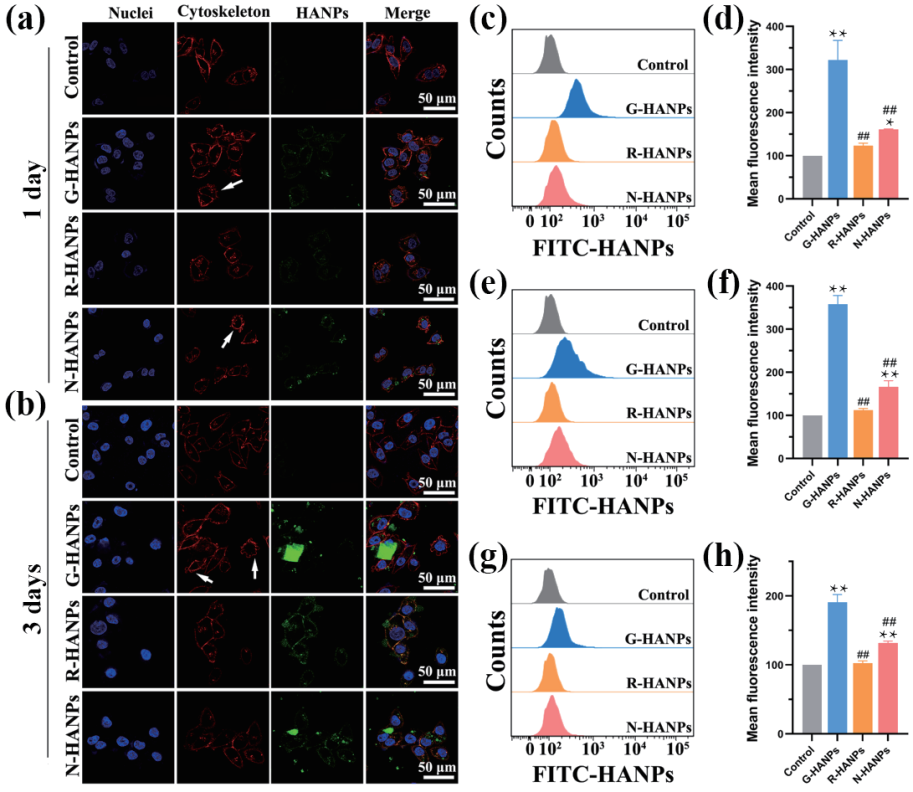

Figure 4 The G-HANPs showed the highest level of intracellular uptake efficiency in the tumor cells. Representative CLSM images of A375 cells stained with nuclei (blue) and cytoskeleton (red) after the cells were treated with the three HANPs labeled with FITC (green) at the concentration of 200 μg/mL for 1 (a) or 3 days (b) (white arrow: vacuoles presented on nuclear membrane). Representative FCM histograms (c), (e), and (g), and MFI (d), (f), and (h) of A375 cells treated with the three FITC-HANPs at the concentration of 200 μg/mL for 4 h (c) and (d), 1 day (e) and (f), and 3 days (g) and (h) (n = 3; vs. Control, $^*P < 0.05$ and $^{**}P < 0.01$; vs. G-HANPs, $^{\#}P < 0.05$ and $^{\#\#}P < 0.01$).

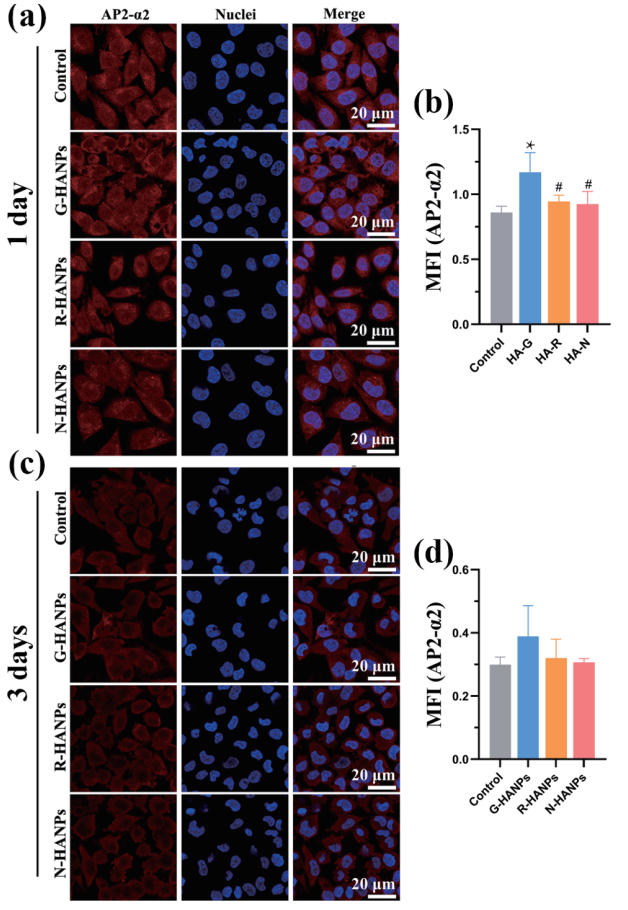

Figure 5 G-HANPs induced a highest level of AP2-α2 in the tumor cells among the three HANPs. Representative CLSM images (a) and (c) and semi-quantitative MFI (b) and (d) of A375 cells stained by nuclei (blue) and fluorescence labeled AP2-α2 antibody (red) after the cells were treated with the three HANPs at the concentration of 200 μg/mL for 1 day (a) and (b) and 3 days (c) and (d) ($n = 3$; vs. Control, $^{*}P < 0.05$ and $^{**}P < 0.01$; vs. G-HANPs, $^{\#}P < 0.05$ and $^{\#\#}P < 0.01$).

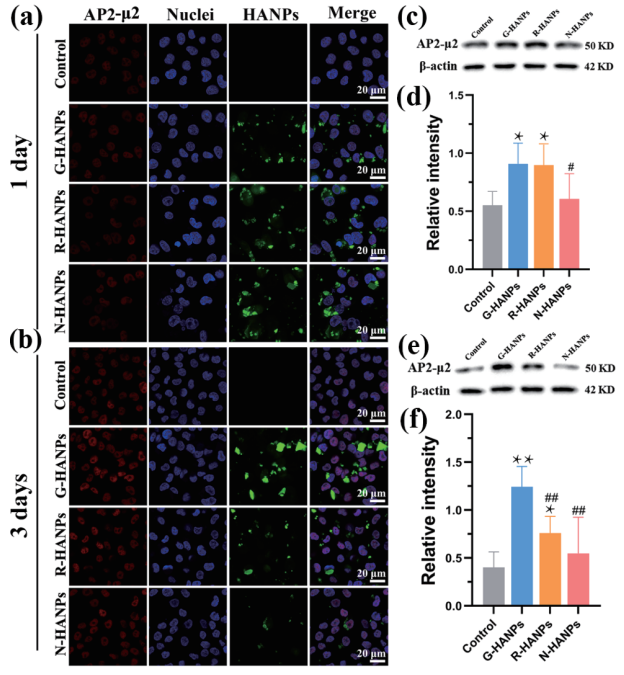

Figure 6 G-HANPs induced a highest level of AP2-μ2 in the tumor cells among the three HANPs. Typical CLSM images of A375 cells stained by nuclei (blue) and fluorescence labeled AP2-μ2 antibody (red) after the cells were treated with the three HANPs labeled with FITC (green) at the concentration of 200 μg/mL for 1 day (a) and 3 days (b). Western blot analysis of AP2-μ2 protein in A375 cells treated with the three HANPs at the concentration of 200 μg/mL for 1 day (c) and (d) and 3 days (e) and (f) ($n = 3$; vs. Control, $^{*}P < 0.05$ and $^{**}P < 0.01$; vs. G-HANPs, $^{\#}P < 0.05$ and $^{\#\#}P < 0.01$).

growth and weight of each mouse were monitored for all groups along with 35 days (Fig. 7(a)). There was no statistical significance for the body weight among all the groups (Fig. 7(b)). But for tumor growth, we observed the tumor appeared at day 5 and sharply grew after 19 days in the control group. During the course of tumor monitoring since day 5 following inoculation, HANPs delayed the tumor growth significantly, compared with the HANPs free groups. Of all the HANPs groups, G-HANPs treatment exhibits the greatest anti-tumor effect (Fig. 7(c)).

At day 35, the tumor was excised from the tumor-bearing mice and weighed. The results showed that the tumor weight and volume in the three HANPs groups were lower than those in the control group. Among the three HANPs, G-HANPs presented the best anti-tumor efficiency (Figs. 7(d)–7(f)). These results indicated that the anti-tumor effect of HANPs could be controlled by their morphologies. And the G-HANPs presented the best anti-tumor effect among the studied three shapes of HANPs.

3.6 Histopathology analysis of the resected tumor tissues *in vivo*

We next analyzed the histopathology of the tumor tissues from the mice treated with or without the three HANPs to further confirm the above results and investigate the expression of AP2-μ2 by H&E and immunohistochemistry staining. The H&E staining results showed that the cells in the control group were closely arranged in sheets and showed heterogeneous nuclei, which were the typical tumor cell morphologies (Fig. 8(a) and Fig. S3 in the ESM). Meanwhile, a highly expressed level of Ki-67 as a proliferation marker for tumor cells and CD31 known as platelet/endothelial cell adhesion molecule were observed in the control group (Figs. 8(a) and 8(b)). However, the tumor tissues treated with HANPs were found varying degrees of nuclear shrinkage and loose tissue structure, a decelerated level of Ki-67, increased levels of TUNEL and AP2-μ2 protein, and impaired CD31 expression (Figs. 8(a) and 8(b)). These results supported the above evidences that all the three HANPs inhibited tumor growth and G-HANPs exhibited the most prominent tumor inhibition effect, as indicated by the lowest expression levels of Ki-67 and CD31 and highest levels of TUNEL and AP2-μ2 protein.

At day 35, the heart, liver, spleen, lung, and kidney of all the three HANPs tumor-bearing mice showed normal tissue morphology, and no inflammatory cell infiltrations or HANPs were observed in these organs (Fig. S4(a) in the ESM). Compared with the control group, the blood routine data of the three experimental groups showed no statistical difference (Table S1 in the ESM). All the blood biochemical parameters of liver function, kidney function, and electrolytes including ALT, AST, CREA, urea, Ca, and P showed that there was no significant difference between the three experimental groups and the control group (Fig. S4(b) in the ESM). In conclusion, HANPs is a kind of nanomaterial with good biosafety.

4 Discussion

The purpose of this study was to investigate how the morphology of HANPs impacts the endocytosis of the particles in human melanoma cells and their anti-tumor effect *in vivo*. The results demonstrated that compared with R-HANPs or N-HANPs, G-HANPs was the most efficient to up-regulate the expression level of AP2 protein in the tumor cells and delay tumor growth *in vivo*. This study offers an insight into the interaction between the

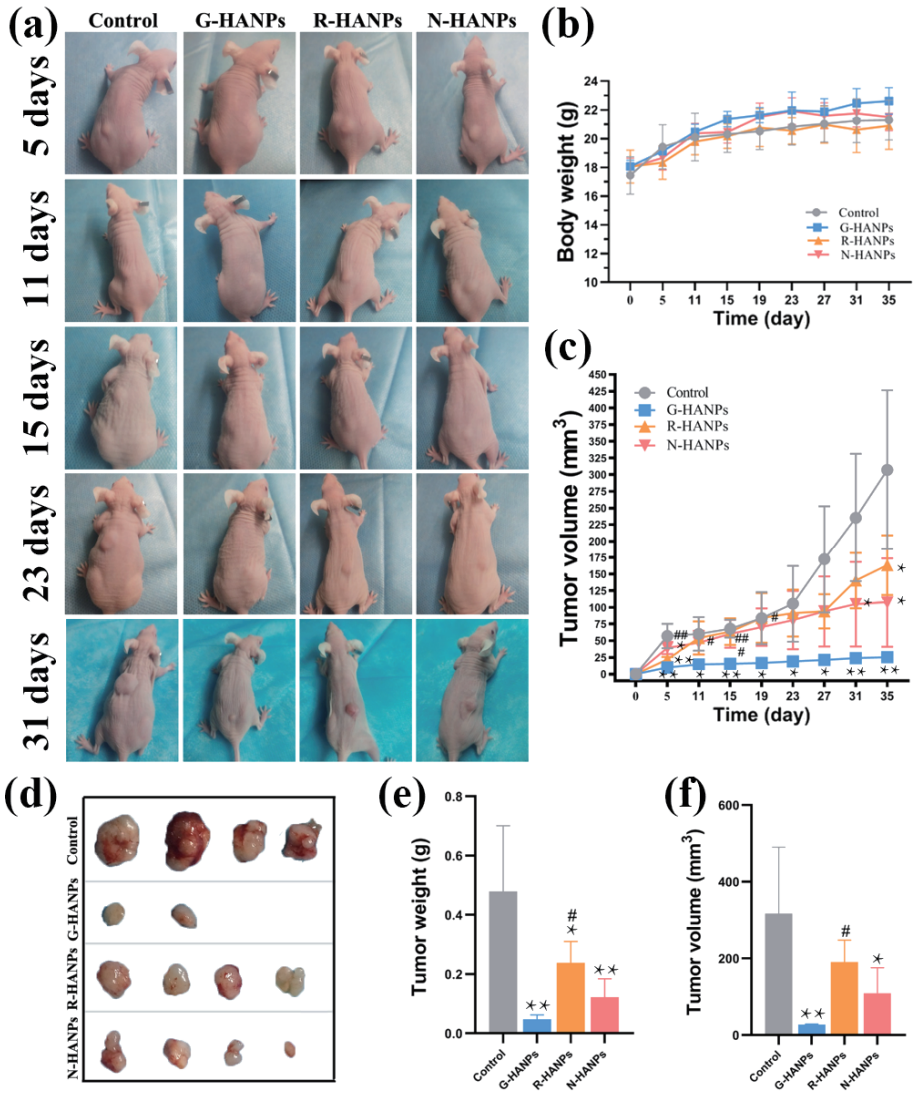

Figure 7 The G-HANPs delayed tumor growth most efficiently among the three HANPs. Macroscopic observation for the growth of the tumor tissues in A375 melanoma-bearing mice (a). The changes of body weight (b) and tumor volume (c) of A375 melanoma-bearing mice after inoculation (vs. Control, $^{*}P < 0.05$ and $^{**}P < 0.01$; vs. G-HANPs, $^{\#}P < 0.05$ and $^{\#\#}P < 0.01$). Representative tumor photos resected from A375 melanoma-bearing mice at day 35 (d). The quantitative analysis of the resected tumor weight (e) and tumor volume (f) at day 35 (vs. Control, $^{*}P < 0.05$ and $^{**}P < 0.01$; vs. G-HANPs, $^{\#}P < 0.05$ and $^{\#\#}P < 0.01$).

morphology of HANPs and AP2 protein, which will support the rational design of the nanomaterials for efficient tumor therapy.

In recent years, HANPs have been widely used in biomedical fields and tumor treatment, and applied as bone repair materials and drug delivery carriers [1–7]. A number of studies have showed that HANPs selectively inhibits the proliferation of tumor cells, but has little or even no inhibitory effect on the growth of normal cells, including fibroblasts [4, 7], mesenchymal stem cells [6, 12], hepatocytes [31, 32], etc. The mechanism by which HANPs inhibit tumor growth involves the increased intracellular Ca^{2+} levels in the tumor cells, which leads to mitochondria apoptosis. Previous studies had shown that the increase of intracellular Ca^{2+} had a crucial impact on the morphological change of mitochondria, which potentially involved the apoptosis of tumor cells [9, 10]. Ca^{2+} is an important second messenger that exists widely in cells and plays an important regulatory role in the proliferation, differentiation, and migration of tumor cells [33–35]. A lot of studies reported that the homeostasis imbalance of Ca^{2+} led to abnormal function of tumor cells and promoted apoptosis of tumor cells [36–38]. He et al. revealed that Ca^{2+} release inhibited the proliferation of ocular melanoma [39].

The amount of released Ca^{2+} from HANPs increased in acidic solution (pH = 5.5), compared with that in neutral solution (pH = 7.4) (Fig. S1 in the ESM). It is reasonable that the HANPs represented as Ca^{2+} store, which could elevate intracellular Ca^{2+} level especially when they encountered the acidic lysosome in the tumor cells. In the present study, the cellular TEM images indicate that all HANPs regardless of their morphologies could enter the tumor cells, and increase the level of intracellular Ca^{2+} (Fig. 3). Interestingly, among all the three HANPs, the G-HANPs elicited a highest level of intracellular Ca^{2+} and were the only HANPs induced the swelling of mitochondria, as well as the loss of $\Delta\psi_m$ (Fig. 3). The morphology-dependent effect might involve the endocytosis efficiency of HANPs. This is further validated by the quantitative analysis of intracellular uptake assay, which showed that the three labeled HANPs could be effectively internalized into A375 cells, and the G-HANPs entered the cells most efficiently (Fig. 4). Therefore, the morphology of HANPs linked with their endocytosis efficiency and the scale of their function to induce mitochondria apoptosis.

Currently, the endocytosis for nanoparticles is considered to be a two-step process: The nanoparticles are bound to the cell surface and then absorbed through specific endocytosis pathways [40]. Some studies showed that HANPs entered tumor cells mainly through CME. CME of nanoparticles is closely related to the size of particles, and small size particles can be more effectively

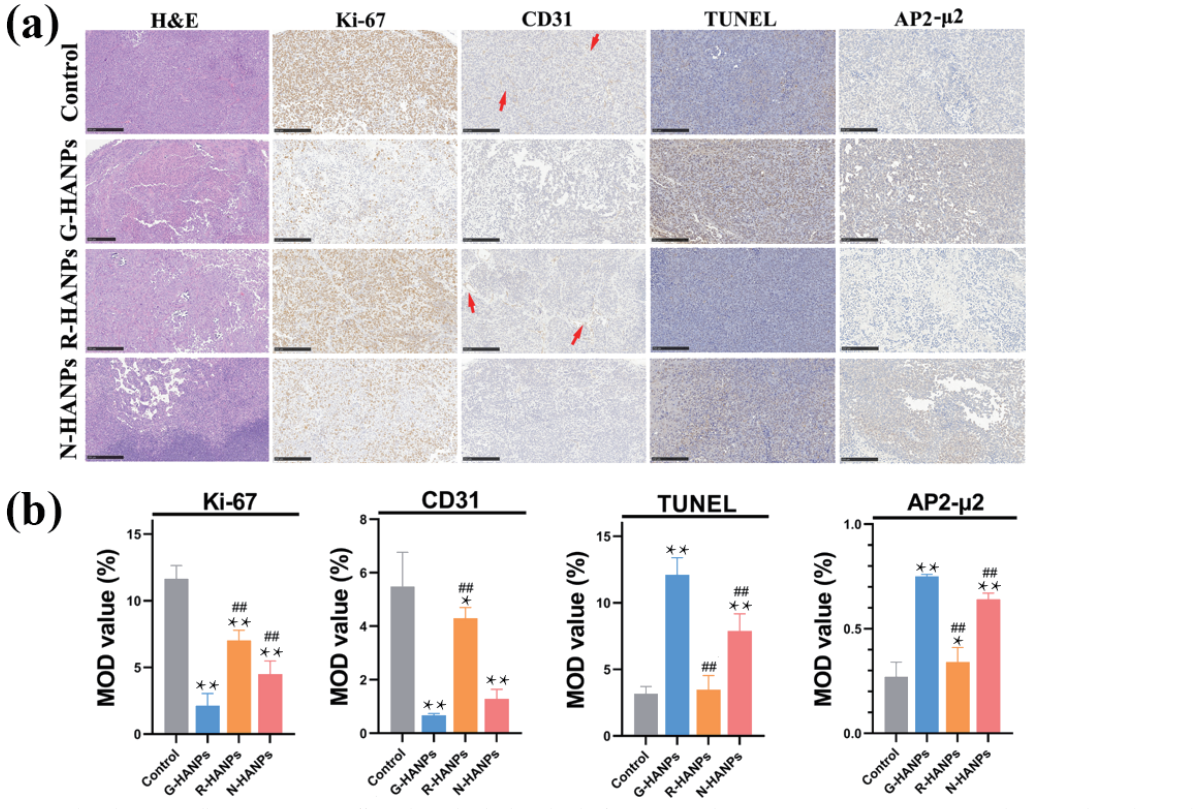

Figure 8 G-HANPs induced tumor cell apoptosis most efficiently and a highest level of AP2-μ2 in the tumor tissues. H&E staining and immunohistochemical staining of Ki-67, CD31, TUNEL, and AP2-μ2 of the resected tumor tissues at day 35 (red arrow: blood vessel, scale bars: 250 μm) (a). The semi-quantification of Ki-67, CD31, TUNEL, and AP2-μ2 in the resected tumor tissues after tumor inoculation for 35 days (vs. Control, $^{*}P < 0.05$ and $^{**}P < 0.01$; vs. G-HANPs, $^{\#}P < 0.05$ and $^{\#\#}P < 0.01$) (b).

internalized into cells [41–44]. Shi et al. found that 20 nm HANPs were more effective for the induction of cell apoptosis than 80 nm HANPs [44]. The morphology of nanoparticles is another important factor that directly influences their endocytosis [45–47]. Chithrani et al. found that spherical nanoparticles entered into cells more easily through CME than rod-like NPs [45]. So far, there has been a certain research progress on the anti-tumor effect of HANPs and the CME between HANPs and tumor cells [6, 7, 9, 10]. Cui et al. discovered that CME and vesicle-mediated endocytosis were involved in the cellular uptake of various HANPs [10]. It was confirmed in our study that CME pathway mediated the endocytosis of HANPs into A375 cells (Fig. S2 in the ESM). AP2 is a class of proteins that play an important role in cargo identification in CME. The protein is mainly located in the plasma membrane as a transport connector, and is critical in many intracellular vesicle transport pathways [18–20, 23, 48, 49]. Zhu et al. recently investigated the effect of the morphology of HANPs on the interaction between the AP2 protein and the particles using molecular dynamics simulation method. They found spherical HANPs and N-HANPs had specific binding sites with AP2-μ2, which caused different conformational changes of the proteins. However, rod-like HANPs was rapidly isolated from AP2-μ2, keeping distance from the protein. Spherical HANPs might promote their more profound tumor inhibition by transferring AP2-μ2 to the locked conformation [24]. In this study we found that compared with R-HANPs or N-HANPs, G-HANPs induced a higher expression level of AP2 protein by co-culture of HANPs and tumor cells (Figs. 5 and 6) or in the HANPs treated tumor mouse model (Fig. 8). These results demonstrated that the endocytosis signaling could be regulated by the morphology of HANPs.

In the A375 melanoma-bearing Balb/c nude mouse model, we found that tumor growth was delayed by all the three HANPs, among which, G-HANPs showed the greatest effect on the inhibition of tumor growth and the up-regulation of AP2 protein levels in the tumor tissues (Figs. 7 and 8), wihch was consistent with the results from the *in vitro* experiments. In the tumor tissues, the up-regulation of AP2 protein expression by HANPs might not be limited to tumor cells, which remained to be further investigated. These results demonstrated that the morphology of HANPs influenced the endocytosis signaling and thereby contributed to the different effect on tumor growth inhibition. Additionally, we further found that these HANPs had no obvious toxicity to the mice, confirming HANPs had good biocompatible properties (Fig. S4 and Table S1 in the ESM).

5 Conclusions

In summary, the present study demonstrated that the morphology of HANPs regulated their endocytosis efficiency in tumor cells and their anti-tumor effect *in vivo*. Among G-HANPs, R-HANPs, and N-HANPs, the G-HANPs was the most efficient for the internalization of the particles into melanoma cells, elevation of the expression level of AP2 protein, and inhibition of tumor growth in the tumor-bearing mouse model. In addition, all the three HANPs had good biosafety when applied *in vivo*. The present study could contribute to the rational design of the intracellular nanomaterials for anti-tumor study.

Acknowledgements

This work was supported by Sichuan Science and Technology Program (No. 2020YFS0039), the National Natural Science Foundation of China (No. 81901685), and the Fundamental Research Funds for the Central Universities (No. YJ201915).

Electronic Supplementary Material: Supplementary material

(experimental, analysis, and computational details, SEM, TEM, and STEM images, XRD patterns, XPS spectra, and CV and LSV curves) is available in the online version of this article at https://doi.org/10.1007/s12274-022-4220-y.

References

[1] Tang, Z. R.; Li, X. F.; Tan, Y. F.; Fan, H. S.; Zhang, X. D. The material and biological characteristics of osteoinductive calcium phosphate ceramics. *Regen. Biomater.* **2017**, *5*, 43–59.

[2] Hong, Y. L.; Fan, H. S.; Li, B.; Guo, B.; Liu, M.; Zhang, X. D. Fabrication, biological effects, and medical applications of calcium phosphate nanoceramics. *Mater. Sci. Eng. R Rep.* **2010**, *70*, 225–242.

[3] Ribeiro, N.; Sousa, S. R.; Van Blitterswijk, C. A.; Moroni, L.; Monteiro, F. J. A biocomposite of collagen nanofibers and nanohydroxyapatite for bone regeneration. *Biofabrication* **2014**, *6*, 035015.

[4] Li, Z. T.; Tang, J. Q.; Wu, H. F.; Ling, Z. X.; Chen, S. Y.; Zhou, Y.; Guo, B.; Yang, X.; Zhu, X. D.; Wang, L. et al. A systematic assessment of hydroxyapatite nanoparticles used in the treatment of melanoma. *Nano Res.* **2020**, *13*, 2106–2117.

[5] Zhang, K.; Zhou, Y.; Xiao, C.; Zhao, W. L.; Wu, H. F.; Tang, J. Q.; Li, Z. T.; Yu, S.; Li, X. F.; Min, L. et al. Application of hydroxyapatite nanoparticles in tumor-associated bone segmental defect. *Sci. Adv.* **2019**, *5*, eaax6946.

[6] Zhao, H.; Wu, C. H.; Gao, D.; Chen, S. P.; Zhu, Y. D.; Sun, J.; Luo, H. R.; Yu, K.; Fan, H. S.; Zhang, X. D. Antitumor effect by hydroxyapatite nanospheres: Activation of mitochondria-dependent apoptosis and negative regulation of phosphatidylinositol-3-kinase/protein kinase B pathway. *ACS Nano* **2018**, *12*, 7838–7854.

[7] Wu, H. F.; Li, Z. T.; Tang, J. Q.; Yang, X.; Zhou, Y.; Guo, B.; Wang, L.; Zhu, X. D.; Tu, C. Q.; Zhang, X. D. The *in vitro* and *in vivo* anti-melanoma effects of hydroxyapatite nanoparticles: Influences of material factors. *Int. J. Nanomedicine* **2019**, *14*, 1177–1191.

[8] Aoki, H.; Ohgaki, M.; Kano, S. Effects of adriacin-absorbing hydroxyapatite-sol on Ca-9 cell growth. *Rep. Inst. Med. Dent. Eng.* **1993**, *27*, 39–44.

[9] Chu, S. H.; Feng, D. F.; Ma, Y. B.; Li, Z. Q. Hydroxyapatite nanoparticles inhibit the growth of human glioma cells *in vitro* and *in vivo*. *Int. J. Nanomedicine* **2012**, *7*, 3659–3666.

[10] Cui, X. H.; Liang, T.; Liu, C. S.; Yuan, Y.; Qian, J. C. Correlation of particle properties with cytotoxicity and cellular uptake of hydroxyapatite nanoparticles in human gastric cancer cells. *Mater. Sci. Eng. C* **2016**, *67*, 453–460.

[11] Wang, Y. F.; Wang, J. L.; Hang, H.; Cai, M. L.; Wang, S. Y.; Ma, J.; Li, Y.; Mao, C. B.; Zhang, S. M. *In vitro* and *in vivo* mechanism of bone tumor inhibition by selenium-doped bone mineral nanoparticles. *Acs Nano* **2016**, *10*, 9927–9937.

[12] Li, X.; Wang, Y. F.; Chen, Y.; Zhou, P.; Wei, K.; Wang, H.; Wang, J. L.; Fang, H.; Zhang, S. M. Hierarchically constructed selenium-doped bone-mimetic nanoparticles promote ros-mediated autophagy and apoptosis for bone tumor inhibition. *Biomaterials* **2020**, *257*, 120253.

[13] Kirchhausen, T.; Owen, D.; Harrison, S. C. Molecular structure, function, and dynamics of clathrin-mediated membrane traffic. *Cold Spring Harb. Perspect. Biol.* **2014**, *6*, a016725.

[14] Kovtun, O.; Dickson, V. K.; Kelly, B. T.; Owen, D. J.; Briggs, J. A. G. Architecture of the AP2: Clathrin coat on the membranes of clathrin-coated vesicles. *Sci. Adv.* **2020**, *6*, eaba8381.

[15] Mettlen, M.; Chen, P. H.; Srinivasan, S.; Danuser, G.; Schmid, S. L. Regulation of clathrin-mediated endocytosis. *Annu. Rev. Biochem.* **2018**, *87*, 871–896.

[16] Reis, C. R.; Chen, P. H.; Bendris, N.; Schmid, S. L. TRAIL-death receptor endocytosis and apoptosis are selectively regulated by dynamin-1 activation. *Proc. Natl. Acad. Sei. USA* **2017**, *114*, 504–509.

[17] Mcmahon, H. T.; Boucrot, E. Molecular mechanism and physiological functions of clathrin-mediated endocytosis. *Nat. Rev. Mol. Cell Biol.* **2011**, *12*, 517–533.

[18] Wood, L. A.; Larocque, G.; Clarke, N. I.; Sarkar, S.; Royle, S. J. New tools for "hot-wiring" clathrin-mediated endocytosis with temporal and spatial precision. *J. Cell Biol.* **2017**, *216*, 4351–4365.

[19] Hayashi, H.; Inamura, K.; Aida, K.; Naoi, S.; Horikawa, R.; Nagasaka, H.; Takatani, T.; Fukushima, T.; Hattori, A.; Yabuki, T. et al. Ap2 adaptor complex mediates bile salt export pump internalization and modulates its hepatocanalicular expression and transport function. *Hepatology* **2012**, *55*, 1889–1900.

[20] Robinson, M. S. Forty years of clathrin-coated vesicles. *Traffic* **2015**, *16*, 1210–1238.

[21] Pearse, B. M.; Robinson, M. S. Purification and properties of 100-kd proteins from coated vesicles and their reconstitution with clathrin. *EMBO J.* **1984**, *3*, 1951–1957.

[22] Schmid, E. M.; Ford, M. G. J.; Burtey, A.; Praefcke, G. J. K.; Peak-Chew, S. Y.; Mills, I. G.; Benmerah, A.; Mcmahon, H. T. Role of the ap2 β-appendage hub in recruiting partners for clathrin-coated vesicle assembly. *PLoS Biol.* **2006**, *4*, e262.

[23] Wang, X. X.; Chao, Y. Z.; Wang, Y.; Xu, B. H.; Wang, C.; Li, H. Identification of an adaptor protein-2 mu gene (*AccAp2m*) in *Apis cerana cerana* and its role in oxidative stress responses. *J. Cell. Biochem.* **2019**, *120*, 16600–16613.

[24] Zhu, C.; Zhou, X. J.; Liu, Z. T.; Chen, H. W.; Wu, H. F.; Yang, X.; Zhu, X. D.; Ma, J.; Dong, H. The morphology of hydroxyapatite nanoparticles regulates cargo recognition in clathrin-mediated endocytosis. *Front. Mol. Biosci.* **2021**, *8*, 627015.

[25] Gratton, S. E. A.; Ropp, P. A.; Pohlhaus, P. D.; Luft, J. C.; Madden, V. J.; Napier, M. E.; Desimone, J. M. The effect of particle design on cellular internalization pathways. *Proc. Natl. Acad. Sci. USA* **2008**, *105*, 11613–11618.

[26] Setyawati, M. I.; Tay, C. Y.; Chia, S. L.; Goh, S. L.; Fang, W.; Neo, M. J.; Chong, H. C.; Tan, S. M.; Loo, S. C. J.; Ng, K. W. et al. Titanium dioxide nanomaterials cause endothelial cell leakiness by disrupting the homophilic interaction of VE-cadherin. *Nat. Commun.* **2013**, *4*, 1673.

[27] Tomayko, M. M.; Reynolds, C. P. Determination of subcutaneous tumor size in athymic (nude) mice. *Cancer Chemother. Pharmacol.* **1989**, *24*, 148–154.

[28] Medina, P. P.; Nolde, M.; Slack, F. J. Oncomir addiction in an *in vivo* model of microRNA-21-induced pre-B-cell lymphoma. *Nature* **2010**, *467*, 86–90.

[29] Zhang, M. J.; Liu, S. N.; Xu, G.; Guo, Y. N.; Zhang, D. C. Cytotoxicity and apoptosis induced by nanobacteria in human breast cancer cells. *Int. J. Nanomedicine* **2014**, *9*, 265–271.

[30] Emanuele, S.; Lauricella, M.; Carlisi, D.; Vassallo, B.; D'Anneo, A.; Di Fazio, P.; Vento, R.; Tesoriere, G. Saha induces apoptosis in hepatoma cells and synergistically interacts with the proteasome inhibitor bortezomib. *Apoptosis* **2007**, *12*, 1327–1338.

[31] Tang, W.; Yuan, Y.; Liu, C. S.; Wu, Y. Q.; Qian, J. C. Differential cytotoxicity and particle action of hydroxyapatite nanoparticles in human cancer cells. *Nanomedicine* **2013**, *9*, 397–412.

[32] Han, Y. C.; Li, S. P.; Cao, X. Y.; Yuan, L.; Wang, Y. F.; Yin, Y. X.; Qiu, T.; Dai, H. L.; Wang, X. Y. Different inhibitory effect and mechanism of hydroxyapatite nanoparticles on normal cells and cancer cells *in vitro* and *in vivo*. *Sci. Rep* **2014**, *4*, 7134.

[33] Humeau, J.; Pedro, J. M. B. S.; Vitale, I.; Nuñez, L.; Villalobos, C.; Kroemer, G.; Senovilla, L. Calcium signaling and cell cycle: Progression or death. *Cell Calcium* **2018**, *70*, 3–15.

[34] An, J. Y.; Zhang, K. X.; Wang, B. H.; Wu, S. X.; Wang, Y. F.; Zhang, H. L.; Zhang, Z. Z.; Liu, J. J.; Shi, J. J. Nanoenabled disruption of multiple barriers in antigen cross-presentation of dendritic cells via calcium interference for enhanced chemo-immunotherapy. *ACS Nano* **2020**, *14*, 7639–7650.

[35] Bong, A. H. L.; Monteith, G. R. Calcium signaling and the therapeutic targeting of cancer cells. *Biochim. Biophys. Acta Mol. Cell Res.* **2018**, *1865*, 1786–1794.

[36] Cao, R.; Sun, W.; Zhang, Z.; Li, X. J.; Du, J. J.; Fan, J. L.; Peng, X. J. Protein nanoparticles containing Cu(II) and DOX for efficient chemodynamic therapy via self-generation of H_2O_2. *Chin. Chem. Lett.* **2020**, *31*, 3127–3130.

[37] Lin, L. S.; Huang, T.; Song, J. B.; Ou, X. Y.; Wang, Z. T.; Deng, H. Z.; Tian, R.; Liu, Y. J.; Wang, J. F.; Liu, Y. et al. Synthesis of copper peroxide nanodots for H_2O_2 self-supplying chemodynamic therapy. *J. Am. Chem. Soc.* **2019**, *141*, 9937–9945.

[38] Dong, S.; Chen, Y.; Yu, L.; Lin, K.; Wang, X. Magnetic

hyperthermia-synergistic H_2O_2 self-sufficient catalytic suppression of osteosarcoma with enhanced bone-regeneration bioactivity by 3D-printing composite scaffolds. *Adv. Funct. Mater.* **2020**, *30*, 1907071.

[39] He, F. L.; Yu, J.; Yang, J.; Wang, S. Y.; Zhuang, A.; Shi, H. H.; Gu, X.; Xu, X. F.; Chai, P. W.; Jia, R. B. m^6A RNA hypermethylation-induced BACE2 boosts intracellular calcium release and accelerates tumorigenesis of ocular melanoma. *Mol. Ther.* **2021**, *29*, 2121–2133.

[40] Kumari, A.; Yadav, S. K. Cellular interactions of therapeutically delivered nanoparticles. *Expert Opin. Drug Deliv.* **2011**, *8*, 141–151.

[41] Zhang, S. L.; Li, J.; Lykotrafitis, G.; Bao, G.; Suresh, S. Size-dependent endocytosis of nanoparticles. *Adv. Mater.* **2010**, *21*, 419–424.

[42] Aoyama, Y.; Kanamori, T.; Nakai, T.; Sasaki, T.; Horiuchi, S.; Sando, S.; Niidome, T. Artificial viruses and their application to gene delivery. size-controlled gene coating with glycocluster nanoparticles. *J. Am. Chem. Soc.* **2003**, *125*, 3455–3457.

[43] Gao, H. J.; Shi, W. D.; Freund, L. B. Mechanics of receptor-mediated endocytosis. *Proc. Natl. Acad. Sci. USA* **2005**, *102*, 9469–9474.

[44] Shi, Z. L.; Huang, X.; Cai, Y. R.; Tang, R. K.; Yang, D. S. Size effect of hydroxyapatite nanoparticles on proliferation and apoptosis of osteoblast-like cells. *Acta Biomater.* **2009**, *5*, 338–345.

[45] Chithrani, B. D.; Chan, W. C. W. Elucidating the mechanism of cellular uptake and removal of protein-coated gold nanoparticles of different sizes and shapes. *Nano Lett.* **2007**, *7*, 1542–1550.

[46] Chithrani, B. D.; Ghazani, A. A.; Chan, W. C. W. Determining the size and shape dependence of gold nanoparticle uptake into mammalian cells. *Nano Lett.* **2006**, *6*, 662–668.

[47] Qiu, Y.; Liu, Y.; Wang, L. M.; Xu, L. G.; Bai, R.; Ji, Y. L.; Wu, X. C.; Zhao, Y. L.; Li, Y. F.; Chen, C. Y. Surface chemistry and aspect ratio mediated cellular uptake of au nanorods. *Biomaterials* **2010**, *31*, 7606–7619.

[48] Gulbranson, D. R.; Crisman, L.; Lee, M. S.; Ouyang, Y.; Menasche, B. L.; Demmitt, B. A.; Wan, C.; Nomura, T.; Ye, Y. H.; Yu, H. J. et al. AAGAB controls AP2 adaptor assembly in clathrin-mediated endocytosis. *Dev. Cell* **2019**, *50*, 436–446, e5.

[49] Partlow, E. A.; Baker, R. W.; Beacham, G. M.; Chappie, J. S.; Leschziner, A. E.; Hollopeter, G. A structural mechanism for phosphorylation-dependent inactivation of the AP2 complex. *eLife* **2019**, *8*, e50003.